

Spectral broadening in anatase titanium dioxide waveguides at telecommunication and near-visible wavelengths

Christopher C. Evans,¹ Katia Shtyrkova,² Jonathan D. B. Bradley,^{1,2}
Orad Reshef,¹ Erich Ippen,² and Eric Mazur^{1,*}

¹*School of Engineering and Applied Sciences, Harvard University, 9 Oxford Street,
Cambridge, Massachusetts 02138 USA*

²*Department of Electrical Engineering and Computer Science, Massachusetts Institute of
Technology, 77 Massachusetts Avenue, Cambridge, Massachusetts 02139 USA*

* mazur@seas.harvard.edu

Abstract: We observe spectral broadening of femtosecond pulses in single-mode anatase-titanium dioxide (TiO₂) waveguides at telecommunication and near-visible wavelengths (1565 and 794 nm). By fitting our data to nonlinear pulse propagation simulations, we quantify nonlinear optical parameters around 1565 nm. Our fitting yields a nonlinear refractive index of $0.16 \times 10^{-18} \text{ m}^2/\text{W}$, no two-photon absorption, and stimulated Raman scattering from the 144 cm⁻¹ Raman line of anatase with a gain coefficient of $6.6 \times 10^{-12} \text{ m/W}$. Additionally, we report on asymmetric spectral broadening around 794 nm. The wide wavelength applicability and negligible two-photon absorption of TiO₂ make it a promising material for integrated photonics.

© 2013 Optical Society of America

OCIS codes: (190.4390) Integrated optics; (190.4400) Materials; (320.6629) Supercontinuum generation.

References and links

1. V. R. Almeida, C. A. Barrios, R. R. Panepucci, and M. Lipson, "All-optical control of light on a silicon chip," *Nature* **431**, 1081–1084 (2004).
2. P. P. Absil, J. V. Hryniewicz, B. E. Little, P. S. Cho, R. A. Wilson, L. G. Joneckis, and P. T. Ho, "Wavelength conversion in GaAs micro-ring resonators," *Opt. Lett.* **25**, 554–556 (2000).
3. M. A. Foster, A. C. Turner, R. Salem, M. Lipson, and A. L. Gaeta, "Broad-band continuous-wave parametric wavelength conversion in silicon nanowaveguides," *Opt. Express* **15**, 12949–12958 (2007).
4. V. G. Ta'eed, N. J. Baker, L. B. Fu, K. Finsterbusch, M. R. E. Lamont, D. J. Moss, H. C. Nguyen, B. J. Eggleton, D. Y. Choi, S. Madden, and B. Luther-Davies, "Ultrafast all-optical chalcogenide glass photonic circuits," *Opt. Express* **15**, 9205–9221 (2007).
5. A. A. Savchenkov, A. B. Matsko, W. Liang, V. S. Ilchenko, D. Seidel, and L. Maleki, "Kerr combs with selectable central frequency," *Nat. Photon* **5**, 293–296 (2011).
6. Y. Okawachi, K. Saha, J. S. Levy, Y. H. Wen, M. Lipson, and A. L. Gaeta, "Octave-spanning frequency comb generation in a silicon nitride chip," *Opt. Lett.* **36**, 3398–3400 (2011).
7. M. A. Foster, J. S. Levy, O. Kuzucu, K. Saha, M. Lipson, and A. L. Gaeta, "Silicon-based monolithic optical frequency comb source," *Opt. Express* **19**, 14233–14239 (2011).
8. O. Boyraz and B. Jalali, "Demonstration of a silicon Raman laser," *Opt. Express* **12**, 5269–5273 (2004).
9. C. Xiong, L. G. Helt, A. C. Judge, G. D. Marshall, M. J. Steel, J. E. Sipe, and B. J. Eggleton, "Quantum-correlated photon pair generation in chalcogenide As₂S₃ waveguides," *Opt. Express* **18**, 16206–16216 (2010).

10. S. Azzini, D. Grassani, M. J. Strain, M. Sorel, L. G. Helt, J. E. Sipe, M. Liscidini, M. Galli, and D. Bajoni, "Ultra-low power generation of twin photons in a compact silicon ring resonator," *Opt. Express* **20**, 23100–23107 (2012).
11. M. Pollnau, Y. E. Romanyuk, F. Gardillou, C. N. Borca, U. Griebner, S. Rivier, and V. Petrov, "Double tungstate lasers: From bulk toward on-chip integrated waveguide devices," *IEEE J. Sel. Top. Quantum Electron.* **13**, 661–671 (2007).
12. F. Koyama, "Recent advances of VCSEL photonics," *J. Lightwave Technol.* **24**, 4502–4513 (2006).
13. J. W. Hall and A. Pollard, "Near-infrared spectrophotometry: a new dimension in clinical chemistry," *Clin. Chem.* **38**, 1623–1631 (1992).
14. R. W. Boyd and J. E. Heebner, "Sensitive disk resonator photonic biosensor," *Appl. Opt.* **40**, 5742–5747 (2001).
15. H. Obrig and A. Villringer, "Beyond the visible—imaging the human brain with light," *J. Cerebr. Blood F. Met.* **23**, 1–18 (2003).
16. J.-C. G. Bunzli and C. Piguet, "Taking advantage of luminescent lanthanide ions," *Chem. Soc. Rev.* **34**, 1048–1077 (2005).
17. R. H. Hadfield, "Single-photon detectors for optical quantum information applications," *Nat. Photon* **3**, 696–705 (2009).
18. B. S. Wherrett, "Scaling rules for multiphoton interband absorption in semiconductors," *J. Opt. Soc. Am. B* **1**, 67–72 (1984).
19. M. Sheik-Bahae, D. J. Hagan, and E. W. Van Stryland, "Dispersion and band-gap scaling of the electronic Kerr effect in solids associated with two-photon absorption," *Phys. Rev. Lett.* **65**, 96 (1990).
20. M. Dinu, "Dispersion of phonon-assisted nonresonant third-order nonlinearities," *IEEE J. Quantum Electron.* **39**, 1498–1503 (2003).
21. M. Dinu, F. Quochi, and H. Garcia, "Third-order nonlinearities in silicon at telecom wavelengths," *Appl. Phys. Lett.* **82**, 2954–2956 (2003).
22. J. R. M. Osgood, N. C. Panoiu, J. I. Dadap, X. Liu, X. Chen, I. W. Hsieh, E. Dulkeith, W. M. Green, and Y. A. Vlasov, "Engineering nonlinearities in nanoscale optical systems: physics and applications in dispersion-engineered silicon nanophotonic wires," *Adv. Opt. Photon.* **1**, 162–235 (2009).
23. G. I. Stegeman, "Material figures of merit and implications to all-optical waveguide switching," *Proc. SPIE* **1852**, 75–89 (1993).
24. P. Koonath, D. R. Solli, and B. Jalali, "Limiting nature of continuum generation in silicon," *Appl. Phys. Lett.* **93**, 3 (2008).
25. B. J. Eggleton, B. Luther-Davies, and K. Richardson, "Chalcogenide photonics," *Nat. Photon* **5**, 141–148 (2011).
26. J. S. Aitchison, D. C. Hutchings, J. U. Kang, G. I. Stegeman, and A. Villeneuve, "The nonlinear optical properties of AlGaAs at the half band gap," *IEEE J. Quantum Electron.* **33**, 341–348 (1997).
27. G. A. Siviloglou, S. Suntssov, R. El-Ganainy, R. Iwanow, G. I. Stegeman, D. N. Christodoulides, R. Morandotti, D. Modotto, A. Locatelli, C. De Angelis, F. Pozzi, C. R. Stanley, and M. Sorel, "Enhanced third-order nonlinear effects in optical AlGaAs nanowires," *Opt. Express* **14**, 9377–9384 (2006).
28. S. Combrie, Q. V. Tran, A. De Rossi, C. Husko, and P. Colman, "High quality GaInP nonlinear photonic crystals with minimized nonlinear absorption," *Appl. Phys. Lett.* **95**, 221108–3 (2009).
29. J. Pascual, J. Camassel, and H. Mathieu, "Fine structure in the intrinsic absorption edge of TiO₂," *Phys. Rev. B* **18**, 5606 (1978).
30. D. Reyes-Coronado, G. Rodriguez-Gattorno, M. E. Espinosa-Pesqueira, C. Cab, R. d. Coss, and G. Oskam, "Phase-pure TiO₂ nanoparticles: anatase, brookite and rutile," *Nanotechnology* **19**, 145605 (2008).
31. C. C. Evans, J. D. B. Bradley, E. A. Mart-Panameo, and E. Mazur, "Mixed two- and three-photon absorption in bulk rutile (TiO₂) around 800 nm," *Opt. Express* **20**, 3118–3128 (2012).
32. R. Adair, L. L. Chase, and S. A. Payne, "Nonlinear refractive index of optical crystals," *Phys. Rev. B* **39**, 3337 (1989).
33. T. Hashimoto, T. Yoko, and S. Sakka, "Sol-gel preparation and third-order nonlinear optical properties of TiO₂ thin films," *B. Chem. Soc. Jpn* **67**, 653–660 (1994).
34. S. Friberg and P. Smith, "Nonlinear optical glasses for ultrafast optical switches," *IEEE J. Quantum Electron.* **23**, 2089–2094 (1987).
35. H. A. Castillo-Matadamas, R. M. Lima-Garcia, and R. Quintero-Torres, "Ultrafast nonlinear optical properties of TiO₂ nanoclusters at 850 nm," *J. Mod. Opt.* **57**, 1100–1106 (2010).
36. D. Milam, "Review and assessment of measured values of the nonlinear refractive-index coefficient of fused silica," *Appl. Opt.* **37**, 546–550 (1998).
37. S. K. Das, C. Schwanke, A. Pfuch, W. Seeber, M. Bock, G. Steinmeyer, T. Elsaesser, and R. Grunwald, "Highly efficient THG in TiO₂ nanolayers for third-order pulse characterization," *Opt. Express* **19**, 16985–16995 (2011).
38. E. Portuondo-Campa, A. Tortschanoff, F. van Mourik, and M. Chergui, "Ultrafast nonresonant response of TiO₂ nanostructured films," *J. Chem. Phys.* **128**, 244718–10 (2008).
39. H. Long, A. Chen, G. Yang, Y. Li, and P. Lu, "Third-order optical nonlinearities in anatase and rutile TiO₂ thin films," *Thin Solid Films* **517**, 5601–5604 (2009).
40. J. D. B. Bradley, C. C. Evans, J. T. Choy, O. Reshef, P. B. Deotare, F. Parsy, K. C. Phillips, M. Lončar, and

- E. Mazur, "Submicrometer-wide amorphous and polycrystalline anatase TiO₂ waveguides for microphotonic devices," *Opt. Express* **20**, 23821–23831 (2012).
41. J. T. Choy, J. D. B. Bradley, P. B. Deotare, I. B. Burgess, C. C. Evans, E. Mazur, and M. Lončar, "Integrated TiO₂ resonators for visible photonics," *Opt. Lett.* **37**, 539–541 (2012).
 42. V. V. Lozovoy, I. Pastirk, and M. Dantus, "Multiphoton intrapulse interference. IV. Ultrashort laserpulse spectral phase characterization and compensation," *Opt. Lett.* **29**, 775–777 (2004).
 43. G. P. Agrawal, "Quantum electronics—principles and applications," in *Nonlinear fiber optics*, 4th ed. (Elsevier / Academic Press, Amsterdam ; Boston, 2007).
 44. T. Ohsaka, F. Izumi, and Y. Fujiki, "Raman spectrum of anatase, TiO₂," *J. Raman Spectrosc.* **7**, 321–324 (1978).
 45. L. Yin, "Study of Nonlinear Optical Effects in Silicon Waveguides," Ph.D. thesis (2009).
 46. K. J. Blow and D. Wood, "Theoretical description of transient stimulated Raman scattering in optical fibers," *IEEE J. Quantum Electron.* **25**, 2665–2673 (1989).
 47. Q. Lin, O. J. Painter, and G. P. Agrawal, "Nonlinear optical phenomena in silicon waveguides: modeling and applications," *Opt. Express* **15**, 16604–16644 (2007).
 48. K. Ikeda, R. E. Saperstein, N. Alic, and Y. Fainman, "Thermal and Kerr nonlinear properties of plasma-deposited silicon nitride/ silicon dioxide waveguides," *Opt. Express* **16**, 12987–12994 (2008).
 49. M. A. Foster, K. D. Moll, and A. L. Gaeta, "Optimal waveguide dimensions for nonlinear interactions," *Opt. Express* **12**, 2880–2887 (2004).
 50. H. Tang, F. Lvy, H. Berger, and P. E. Schmid, "Urbach tail of anatase TiO₂," *Phys. Rev. B* **52**, 7771 (1995).

1. Introduction

Integrated nonlinear optical devices have enabled many applications for traditional telecommunication wavelengths (1300–1600 nm), ranging from all-optical switches, wavelength converters, amplifiers and lasers, to applications in metrology and quantum information [1–10]. However, few materials are optimal for the unique features of the near-visible window (NVIS, 800–1300 nm). Devices with NVIS compatibility could link and process signals between different communications bands throughout the full communications octave (800–1600 nm) and exploit efficient sources for optical interconnects [11, 12]. Additionally, such devices would open up applications in biology (exploiting the low water absorption in the NVIS) [13–16] and integrated quantum optics (utilizing inexpensive, high-performance silicon single-photon detectors) [17]. Despite their promise, nonlinear optical applications for NVIS wavelengths are almost completely unexplored due to insufficient integrated materials.

Material properties dictate the operating wavelength for optimal performance in all-optical devices. An ideal nonlinear optical material will achieve a maximum effective nonlinearity while minimizing two-photon absorption (2PA) and have a high refractive index to enable strong dispersion engineering for all wavelengths of interest. The nonlinear index of refraction (n_2) depends on the bandgap energy (E_g) and scales as E_g^{-4} , strongly favoring narrow-bandgap materials [18–20]. This bandgap-dependence explains silicon's high nonlinearity ($E_g = 1.1$ eV, $n_2 = 4\text{--}6 \times 10^{-18}$ m²/W [21, 22]). However, strong 2PA in silicon at telecommunication wavelengths limits many all-optical devices [23, 24]. Many materials such as chalcogenide glass [25], AlGaAs [26, 27] and GaInP [28] have excellent nonlinear optical properties for the 1300–1600 nm telecommunication band, yet are limited by 2PA in the NVIS window. For maximum performance at a given operating wavelength, the scaling rules suggest avoiding this limit by selecting a material with bandgap energy of slightly more than twice the single-photon energy. Using these guidelines, we should achieve maximum performance in the NVIS window using a material with a bandgap energy of 3.1 eV.

Titanium dioxide's (TiO₂) unique balance of large optical nonlinearity and wide wavelength compatibility makes it optimal for NVIS operation. TiO₂ exists in several crystalline phases including rutile ($E_g = 3.1$ eV), anatase ($E_g = 3.2$ eV), and brookite ($E_g = 3.1$ eV) making it ideal for wavelengths near 800 nm [29, 30]. The nonlinear index of bulk and thin-film TiO₂ typically ranges from $0.8\text{--}3 \times 10^{-18}$ m²/W in the NVIS window [31–35], which is an order of magnitude greater than the nonlinear index of silica fiber (2.48×10^{-20} m²/W [36]). However,

values obtained from thin-films measurements have been reported as large as $5 \times 10^{-17} \text{ m}^2/\text{W}$ [37], and as small as $1 \times 10^{-19} \text{ m}^2/\text{W}$ [38] and $-6 \times 10^{-17} \text{ m}^2/\text{W}$ [39]. Although there are no reported nonlinearity measurements of bulk anatase, for thin films the value of n_2 for anatase is very similar to that for rutile [33, 39]. The visible transparency and minimal 2PA near 800 nm make TiO_2 most comparable to silicon nitride [1]. However, TiO_2 has a reported Kerr nonlinearity that is over three-times greater than silicon nitride, it possesses a greater refractive index (2.4 versus 2.0), and it can be deposited at low temperatures ($< 400^\circ\text{C}$), allowing for back-end integration with silicon microphotonic devices [31, 40, 41]. Even though TiO_2 is well suited for NVIS applications, integrated nonlinear optical devices in TiO_2 remain undeveloped and unexplored.

In this study, we demonstrate and characterize nonlinear pulse propagation in recently developed anatase TiO_2 waveguides [40]. We observe nonlinear spectral broadening of femtosecond pulses with central wavelengths (λ_0) of 1565 and 794 nm, spanning the communications octave. We fit our measurements to simulations to quantify nonlinear optical parameters and we discuss potential applications for this new material platform. This study represents the first demonstration of optical nonlinearities in integrated TiO_2 devices.

2. Experimental Procedure

We investigate waveguides of various dimensions to ensure strongly confined single-mode operation at widely spaced wavelengths. We fabricate polycrystalline anatase strip-waveguides on silicon substrates with SiO_2 lower cladding and fluoropolymer top cladding using previously reported methods [40]. The waveguides reported here are 250-nm high, have top-widths of 900 and 200 nm, and are 9 and 6 mm long for measurements at 1565 and 794 nm, respectively. Figure 1(a) shows a typical cross section of a polycrystalline anatase waveguide before applying the top cladding, making evident both the polycrystallinity of the anatase material and the 75° sidewall angle. Figures 1(b) and 1(c), show simulated optical intensity profiles for the waveguides (at 1565 nm and 794 nm, respectively). Our fabricated waveguides are single-mode and strongly confine the light at each wavelength of interest, facilitating measurement and parameter extraction.

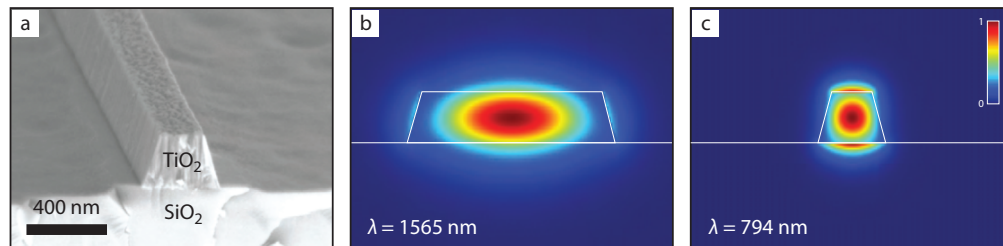


Fig. 1. Scanning electron micrograph of a 200-nm wide polycrystalline-anatase TiO_2 waveguide, prior to top cladding (a). The waveguide is trapezoidal in shape and the TiO_2 grains are columnar in appearance. We show simulated mode-profiles of the fundamental TM and TE-like modes around 1565 and 794 nm (b and c, respectively), showing strong confinement in our single-mode waveguides.

We observe nonlinear pulse propagation by comparing the input versus output spectra of pulses propagating within our waveguides as a function of the input pulse energy. Our measurements are taken with two laser systems: an optical parametric oscillator tuned to 1565 nm and a Ti:Sapphire oscillator centered at 794 nm. We present the laser parameters in Table 1. A half-wave plate followed by a polarizer controls the pulse energy and polarization. We couple into

and out of the waveguides using 0.85 numerical aperture objectives. We measure the output spectra by focusing into a single-mode fiber coupled to an optical spectrum analyzer for 1565 nm and multimode fiber coupled to spectrometer for 794 nm. The shape of the recorded spectra does not change with fiber coupling efficiency, which insures that spectral broadening only occurs within the TiO₂ chips and not within the fibers. Amplitude and phase modulation from a multiphoton intrapulse interference phase scan (MIIPS) system controls the spectrum of the 794 nm pulse and provides a transform-limited duration at the input facet [42]. Even with this correction, we could not form a perfect Gaussian spectral profile. No dispersion compensation was applied for the 1565-nm measurements. The optical propagation losses are 8 and 45 dB/cm measured using the top-view method with coupling efficiencies of −9 and −12 dB/facet calculated from insertion loss measurements (1565 and 794 nm, respectively) [40]. Low-energy spectra are experimentally identical to the input spectra. These low-energy spectra serve as the seed spectra for nonlinear pulse propagation simulation from which we extract nonlinear coefficients.

Table 1. Laser parameters used for measurement.

λ_0 (nm)	repetition rate (MHz)	pulse duration (fs)	max average power (mW)	polarization
1565	80	170	387	TE
794	11	85	18.4	TM

3. Numerical simulation

We quantify the nonlinear optical parameters of anatase TiO₂ by fitting nonlinear pulse propagation simulations to the experimental data. Our simulation solves the generalized nonlinear Schrödinger equation using the slowly varying envelope approximation $A(z, t)$ in the retarded frame, given by:

$$\frac{\partial A(z, t)}{\partial z} + \frac{1}{2} \alpha_1 A(z, t) + \alpha_2 \frac{A^2(z, t)}{A_{\text{eff}}} + \alpha_3 \left(\frac{A^2(z, t)}{A_{\text{eff}}} \right)^2 + \frac{i\beta_2}{2} \frac{\partial^2 A(z, t)}{\partial t^2} - \frac{\beta_3}{6} \frac{\partial^3 A(z, t)}{\partial t^3} = i\gamma \left(1 + \frac{i}{\omega_0} \frac{\partial}{\partial t} \right) \left(A(z, t) \int_{-\infty}^{\infty} R(t') |A(z, t - t')|^2 dt' \right), \quad (1)$$

using the split-step Fourier-transform method [43]. We model linear effects including loss (α_1) and dispersion (β_2 and β_3 , where β_2 is the group velocity dispersion). We model nonlinear effects including self-phase modulation (γ), self-steepening, two- and three-photon absorption (α_2 and α_3 , respectively), and stimulated Raman scattering (through the temporal nonlinear response function $R(t)$). Simulations with and without self-steepening (due to the $\frac{i}{\omega_0} \frac{\partial}{\partial t}$ term) are very similar. In addition, A_{eff} is the effective area for nonlinear absorption. We obtain a noiseless starting spectrum by fitting analytical functions (sech² for 1565 nm and a summation of Gaussians for 794 nm) to the measured low-energy spectrum. For each central wavelength, we calculate linear waveguide parameters that determine light-matter interactions such as the effective area and chromatic dispersion. We extract the nonlinear coefficients by minimizing the mean squared error between simulated and measured data while leaving linear parameters fixed. The values extracted represent a single model that applies to all of the measured data at one wavelength.

Simulating the mode structure of the waveguides allows us to calculate the number of modes and linear waveguide parameters. We determine the energy distributions, $F(x, y)$, and propaga-

tion constants within the waveguide (shown in Figs. 1(b) and 1(c), 1565 and 794 nm, respectively) using a finite-difference eigenmode solver. The 900-nm waveguide only supports a TE mode for $\lambda_0 = 1565$ nm and the 200-nm waveguide supports fundamental TE-like and TM-like modes for $\lambda_0 = 794$ nm, simplifying pulse propagation simulation. Having identified the number and distributions of the modes, we calculate the effective nonlinearity and chromatic dispersion.

The strength of the nonlinear interaction is given by the effective nonlinearity γ , which we calculate from the energy distribution using [43]:

$$\gamma = \frac{2\pi}{\lambda} \frac{\int_{-\infty}^{\infty} n_2(x, y) |F(x, y)|^4 dx dy}{\left(\int_{-\infty}^{\infty} |F(x, y)|^2 dx dy \right)^2}. \quad (2)$$

Using $n_2 = 3 \times 10^{-20}$ m²/W for both silica and the fluoropolymer top cladding and γ determined during fitting, we solve this equation for n_2 in the TiO₂ core. The nonlinearity attributed to the cladding is 10 % for 1565 nm and less than 1 % for 794 nm. Assuming no nonlinear absorption in the cladding, we use a similar expression to calculate effective nonlinear absorption areas, A_{eff} , of 0.43 and 0.16 μm^2 for 1565 nm and 794 nm, respectively [43].

Our model includes the waveguide's group velocity dispersion (GVD), which determines the temporal pulse spreading. GVD reduces the observed nonlinearity for positive (normal) values and leads to complex soliton phenomena for negative (anomalous) values. We calculate the GVD by evaluating the wavelength-dependent propagation constant. We observe lower GVD for the TM mode around 794 nm and therefore conduct all analysis and measurements using TM polarization. The GVD is 1450 and 1480 fs²/mm, corresponding to dispersion parameters $D = -1120$ and -4420 ps/nm/km around 1565 and 794 nm, respectively. The GVD for both waveguides is normal, which enables deterministic broadening and simplifies parameter extraction.

In addition to dispersion and self-phase modulation, the pulse may experience stimulated Raman scattering (SRS), causing photons to scatter inelastically during propagation. It is necessary to add this effect to our simulation because of the strong Raman peaks observed in anatase TiO₂ [44]. The shift (Ω_R), bandwidth (Γ_R), and peak Raman gain (g_R) are characteristic of the waveguide material [43, 45]. In anatase, we expect the 144-cm⁻¹ Raman line to be the dominant source of SRS [44]. The simulation includes SRS as the sum of an instantaneous and a delayed nonlinearity in the temporal nonlinear response function:

$$R(t) = (1 - f_R) \delta(t) + f_R h_R(t), \quad (3)$$

where $R(t)$ is the nonlinear response as a function of time, f_R is the fractional strength of the delayed response, $\delta(t)$ is the Dirac delta function, and $h_R(t)$ is the delayed Raman response function. The Raman gain (g_R) is related to f_R through $f_R = g_R \Gamma_R / (n_2 k_0 \Omega_R)$, where k_0 is the free-space wavevector. We model the Raman response as a Lorentzian using [46]:

$$h_R(t) = \frac{\tau_1^2 + \tau_2^2}{\tau_1 \tau_2} \exp(-t/\tau_2) \sin(t/\tau_1). \quad (4)$$

The parameters τ_1 and τ_2 relate to the frequency shift, $\Omega_R/(2\pi)$, and width, Γ_R/π , of the Raman gain spectrum through $\tau_1 = 1/(\Omega^2 - \Gamma_R^2)^{1/2}$ and $\tau_2 = 1/\Gamma_R$ [43, 45, 47]. By including SRS, this simulation models all linear and nonlinear optical effects expected in our measurements, except for the wavelength-dependence of 2PA, which only occurs near the half-bandgap (775 nm), and third-harmonic generation.

4. Experimental and simulation results

Figure 2 shows measured and simulated spectra for a 900-nm wide anatase TiO₂ waveguide using a 170-fs pulse at $\lambda_0 = 1565$ nm. We present the extracted nonlinear parameters in Table 2. Comparing the lowest and highest energies, we observe broadening by a factor of 3.8, measured –15 dB below the peak. We observe a reasonably good fit for pulse energies up to 229 pJ, while the modulation of the peak at 443 pJ is stronger experimentally than in our simulations.

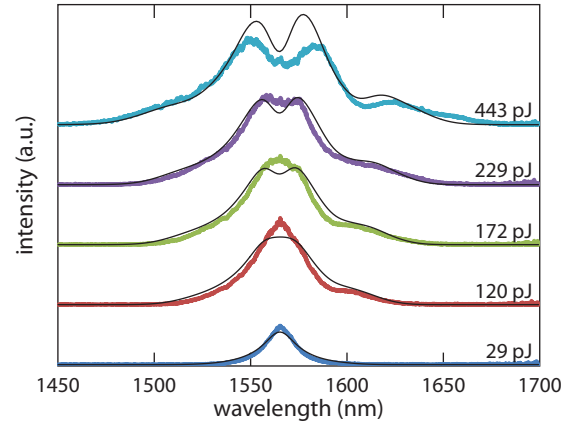


Fig. 2. Measured (thick) and simulated (thin) spectral broadening for a 900-nm wide polycrystalline-anatase TiO₂ waveguide at $\lambda_0 = 1565$ nm at incident energies from 29 pJ to 443 pJ. As the energy is increased, oscillatory features appear in the central peak and a secondary peak around 1600 nm emerges for energies greater than 120 pJ.

We observe two distinct features in the 1565-nm data. First, we see a rounding of the central peak for energies of 172–229 pJ (corresponding to a $3/4$ - π nonlinear phase shift in the simulation) followed by an M-shaped oscillatory structure for 443 pJ. This structure corresponds to a π phase shift in the simulation and is a result of self-phase modulation. Second, we observe an additional asymmetric peak around 1600 nm for a pulse energy of 120 pJ. This peak corresponds to an energy difference of 140 cm^{-1} from the 1565 nm peak and is similar to the 144 cm^{-1} Raman shift in anatase [44]. Therefore, we fix τ_1 to 37 fs to correspond to 144 cm^{-1} . Additionally, the peak red shifts with higher pulse energies, an effect which becomes strongly pronounced at 443 pJ. Setting f_R to zero in the simulation turns off SRS and removes the asymmetric peak while retaining the dominant features in the central peak.

Table 2. Nonlinear optical parameters determined from fitting simulation to experimental data (Figs. 2 and 3). We estimate an uncertainty of $\pm 20\%$ for 1565 nm. Parameters around 794 nm should be considered order of magnitude estimates. Parameters with asterisks were not fit.

λ_0 (nm)	γ (W ⁻¹ m ⁻¹)	n_2 (m ² /W)	α_2 (m/W)	τ_1 (fs)	τ_2 (ps)	f_R
1565	1.5	0.16×10^{-18}	0	37*	1.4	0.18
794	79	1.6×10^{-18}	7×10^{-12}	37*	0.4	0.64

Figure 3 shows measured and simulated spectra for a 200-nm wide anatase TiO₂ waveguide using a 85-fs pulse ($\lambda_0 = 794$ nm) with the simulation parameters shown in Table 2. We were unable to reliably fit all Raman parameters. Consequently, we fix τ_1 to reported bulk values, then fit τ_2 and f_R [44]. The pulse spectrum broadens by a maximum factor of 3.2 for a 56-pJ pulse. Both the output energy and broadening factor saturate at high pulse energy. Turning off 2PA in the simulation removes this saturation. The oscillatory structure that appears in the 794-nm data is more chaotic than the 1565-nm data set. We observe an asymmetry whereby the central peak appears red-shifted; this is much stronger than for 1565 nm. Setting f_R to zero removes the asymmetry in the simulation. The maximum phase shift observed in the simulation is 1.1π . Although the spectral broadening is relatively strong around 794 nm, we are unable to model all the features in the data accurately.

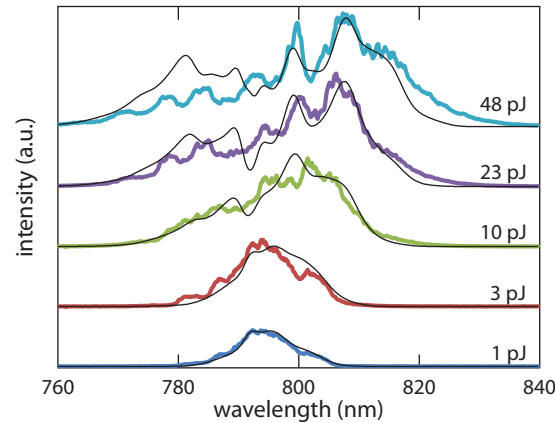


Fig. 3. Measured (thick) and simulated (thin) spectral broadening for a 200-nm wide polycrystalline anatase TiO₂ waveguide at incident energies from 1 pJ to 48 pJ. The data show a strong red-shifted asymmetry with increasing energy at $\lambda_0 = 794$ nm.

5. Discussion

Designing nonlinear optical devices in anatase TiO₂ requires that we understand the distinct features in this new material platform, from nonlinear refraction and absorption to stimulated Raman scattering. We will first focus on the 1565-nm data set, as it has low noise and displays simple features that we can readily model, and then we comment on the 794-nm data set. The largest source of uncertainty is the measured loss ($\pm 50\%$) [40]. Performing a fit using these extremes corresponds to a maximum uncertainty of $\pm 20\%$ for all parameters. The quality of the 1565-nm data set enables reliable parameter extraction that we can use to assess TiO₂'s applicability to all-optical devices.

5.1. Telecommunication wavelengths

Understanding the interplay between nonlinear refraction and absorption in TiO₂ is critical for all-optical devices. Our value of n_2 around 1565 nm (0.16×10^{-18} m²/W) is an order of magnitude lower than typical values for TiO₂ ($0.8\text{--}3 \times 10^{-18}$ m²/W [31–35]). The decreased value of n_2 at telecommunication wavelengths is consistent with theoretical models [19, 20]. In our simulation, we neither expected nor included 2PA at 1565 nm. A small amount of three-photon

absorption ($\alpha_3 = 0.1 \text{ mm}^3/\text{GW}^2$) was included in the model to account for output saturation. We observe a similar trend when using continuous-wave excitation at similar average powers; therefore, this effect may be the result of thermal coupling drift. Our measured value of n_2 is lower in anatase ($0.16 \times 10^{-18} \text{ m}^2/\text{W}$) than for silicon nitride ($0.24 \times 10^{-18} \text{ m}^2/\text{W}$, 1550 nm) [48]. However, the higher linear refractive index of TiO_2 (2.4 in TiO_2 versus 2.0 in silicon nitride) results in stronger confinement and leads to effective nonlinearities (γ) 1.1 times stronger in TiO_2 than in silicon nitride [49]. Our measurement around 1565 nm shows strong effective nonlinearities that are unaffected by 2PA, making TiO_2 a promising material for applications at telecommunication wavelengths.

A high nonlinearity enables maximal nonlinear phase accumulation in devices, however physical effects, such as loss and dispersion, limit the achievable phase shift. The π phase-shift we observe (443-pJ, 1565 nm) is sufficient for distributed feedback gratings, and a 2π phase-shift (needed for a nonlinear Mach-Zehnder interferometer) is achievable with nJ pulses [23]. To reduce this energy requirement, we identify the strongest effects by comparing the length scales at which different effects become relevant. Using the peak power P_0 , pulse duration T_0 , group velocity dispersion β_2 , and the loss α_1 , we calculate a minimum nonlinear length $(\gamma P_0)^{-1}$ of 0.27 mm (443 pJ, 1565 nm), a loss length α_1^{-1} of 5.4 mm, and a dispersion length $T_0^2/|\beta_2|$ of 19 mm. For this 9-mm device, linear loss is the dominant parasitic effect. This loss may be the result of the deposited material's polycrystallinity and sidewall roughness, as seen in Fig. 1(a). Therefore, future research should focus on reducing linear propagation losses. Low-loss TiO_2 waveguides would benefit from dispersion engineering to enable applications such as all-optical switching, four-wave mixing, and supercontinuum generation.

In addition to balancing nonlinear refraction and absorption, SRS is an important effect for all-optical devices. SRS appears as a secondary peak in the 1565-nm data, causing a pronounced asymmetry that we must model when simulating devices. If we perform a second fitting that includes τ_1 , we extract a τ_1 value of 33 fs, which corresponds to a Stokes shift of 161 cm^{-1} ($\Omega_R/(2\pi) = 4.8 \text{ THz}$), which is close to the 144-cm^{-1} line in the spontaneous Raman spectrum and observed in other studies [38]. This energy shift is smaller than silica (402 cm^{-1} , $\tau_1 = 12.2 \text{ fs}$) [46] and silicon (520 cm^{-1} , $\tau_1 = 10.2 \text{ fs}$) [22]. SRS becomes relevant when our pulse bandwidth spans the Raman energy shift and thus, should be included when modeling short pulses ($< 200 \text{ fs}$) in anatase.

The bandwidth and strength of SRS opens up additional applications for TiO_2 . Anatase's crystallinity results in a measured response time of $\tau_2 = 1.4 \text{ ps}$, which is similar to other reported values (1 ps) [38]. This response time corresponds to a bandwidth ($\Gamma_R/\pi = 230 \text{ GHz}$) that is much narrower than amorphous silica (10 THz) and comparable to other crystalline materials such as silicon (105 GHz). Additionally, our extracted value of the Raman fraction, $f_R = 0.18$, is consistent with silica ($f_R = 0.18$) [46] and larger than silicon ($f_R = 0.0664$) [22]. The strength of f_R leads to peak Raman gain coefficients of $6.6 \times 10^{-12} \text{ m/W}$, which is 130 times that of silica ($5 \times 10^{-14} \text{ m/W}$) and an order of magnitude lower than silicon ($2 \times 10^{-10} \text{ m/W}$) [22]. Unlike silicon, the extended transparency of anatase allows Raman amplification throughout the NVIS spectrum, and the narrow shift reduces problems associated with pulse walk-off. The high gain and narrow bandwidth of SRS in anatase may enable ps-pulse and continuous-wave Raman amplifiers, extending into the visible and NVIS windows.

5.2. Near-visible wavelengths

Our 794-nm studies provide the first observation of spectral broadening in TiO_2 waveguides in the NVIS window. Our value of n_2 around 794 nm agrees well with most literature values for the nonlinear index of bulk and thin-film TiO_2 [31–35]. In addition, the wavelength-independent 2PA ($7 \times 10^{-12} \text{ m/W}$) is of the same order of magnitude as that measured in bulk rutile and may

pose a limit for all-optical devices around 800 nm [23, 31]. As was the case with the 1565-nm data set, thermal coupling drift may be the source of the apparent 2PA. Although 2PA may be present, we expect that operating at longer wavelengths (*i.e.*, 850 nm) will eliminate 2PA.

The complex structure and additional un-modeled nonlinear effects increase the uncertainty in our analysis around 794 nm compared to 1565 nm. The intricacies around 794 nm may be a result of the input pulse's structure. The delayed Raman effect attempts to model the asymmetry in the simulation, resulting in an extremely high Raman fraction (0.64), which may be unphysical. This asymmetry may be partially attributed to wavelength-dependent 2PA, which we did not model. This effect is significant in rutile TiO₂ around its half-bandgap (800 nm) [31]. The expected 2PA edge of anatase (775 nm) should not affect the majority of our data, however, a linear absorption (Urbach) tail may extend the linear and nonlinear absorption to lower energies [50]. Alternatively, the crystalline phase may have partially transformed to rutile during fabrication, leading to stronger 2PA for wavelengths shorter than 800 nm. In addition, uncertainties in the input pulse's shape may affect our analysis. We expect that including wavelength-dependent 2PA would reduce the delayed Raman fraction to values similar to those around 1565 nm. The lower quality of the 794-nm data and un-modeled physical processes imply that our analysis should only be considered an order of magnitude estimate, warranting further study in the NVIS spectrum.

6. Conclusion

We observe and quantify spectral broadening in polycrystalline anatase TiO₂ waveguides at two wavelengths ranging from NVIS to telecommunication wavelengths. Using pulse energies of tens to hundreds of pJ, we observe broadening factors greater than 3. Around 1565 nm, the strong effective nonlinearity and the absence of two-photon absorption can facilitate ultrafast, non-resonant all-optical switching applications. Additionally, the small energy shift and high Raman gain of SRS may enable efficient devices such as Raman amplifiers and lasers. The first spectral broadening measurements in the NVIS spectrum show a nonlinearity that agrees well with bulk TiO₂ values. Finally, as we expect little 2PA, we are unable to accurately quantify 2PA in our devices. Based on these first nonlinear results in TiO₂ waveguides, we show that TiO₂ is a promising material for future integrated nonlinear photonics applications throughout the communications octave.

Acknowledgments

Several people contributed to the work described in this paper. C.E. and J.B. conceived of the basic idea for this work. C.E. performed measurements near 800 nm and C.E. and K.S. performed measurements near 1565 nm. C.E. performed the simulations and fitting. J.B. fabricated the waveguides. O.R. aided in the fabrication and the mode simulations. E.M. and E.I. supervised the research and the development of the manuscript. The authors would like to thank Markus Pollnau, Erwin Martí-Panameño, and Ruwan Seneratne for help developing the basis for this work. C.E. wrote the first draft of the manuscript; all authors subsequently took part in the revision process and approved the final copy of the manuscript. Kasey Phillips and Sarah Griesse-Nascimento provided feedback on the manuscript throughout its development. Nonlinear pulse propagation simulations were performed using RP Photonics Fiber Power software. The research described in this paper was supported by the National Science Foundation under contracts ECCS-0901469 and ECCS-1201976, by the MRSEC Program of the National Science Foundation under DMR-0819762, and by AFOSR under FA9550-12-1-0499. C.E. acknowledges support from the Harvard Quantum Optics Center. The authors acknowledge the use of facilities in the Center for Nanoscale Systems, which is supported by the National Science Foundations National Nanotechnology Infrastructure Network.